Compressive Sensing Based Multipath Exploitation for Stationary and Moving Indoor Target Localization

Michael Leigsnering, *Student Member, IEEE,* Fauzia Ahmad, *Senior Member, IEEE,*
Moeness G. Amin, *Fellow, IEEE,* and Abdelhak M. Zoubir, *Fellow, IEEE*

Abstract—Compressive sensing (CS) based multipath exploitation has been successfully applied to stationary indoor scenes in through-the-wall radar imaging (TWRI). The benefits of using significantly reduced data are also desirable for moving targets. Hence, we bring CS based multipath exploitation to the non-stationary target domain and are able to treat moving and stationary targets simultaneously. In general, multipath propagation has adverse effects on the image quality. However, by using proper modeling, multipath can be used to one's advantage. In this paper, we apply CS to both stationary and moving targets under interior wall scatterings. Assuming knowledge of the room geometry, we develop an effective method that solves the inverse problem of joint localization and velocity estimation of the targets in an indoor multipath environment from a few measurements. We also propose a computationally inexpensive scheme that first locates the targets using sparse reconstruction and subsequently estimates the velocity vectors. Effectiveness of the proposed methods is demonstrated using both simulated and experimental data.

Index Terms—Compressive sensing (CS), sparse reconstruction, multipath exploitation, through-the-wall radar imaging (TWRI), Doppler, moving targets.

I. INTRODUCTION

Radar imaging of building interiors has gained much interest due to the rising use in civilian, security, and defense applications [1]–[9]. Through-the-wall radar imaging (TWRI) has the ability to reveal stationary and moving targets behind walls, thereby greatly improving situational awareness in urban areas for the said applications.

The TWRI objective of acquiring precise information on target location and velocity is challenged by multipath propagation due to secondary reflections at interior walls. This results in heavy multipath associated with the target. Specular multipath causes "ghosts" in the imaged scene which stem from the energy being focused at non-target locations. Also, the front wall may cause additional ghosts due to multiple reflections inside the wall. This so-called wall ringing multipath leads to a sequence of target replicas, equally spaced in range, located behind the target. Instead of treating multipath

as clutter, it is prudent to utilize the energy and information contained in these additional target returns. This is usually referred to as multipath exploitation. Another issue is the large amount of data that needs to be acquired, stored and processed to obtain highly resolved images of the scene using conventional approaches, such as backprojection. This calls for an efficient, logistically viable data acquisition scheme to reduce the recording time and system cost.

The above outlined challenges have been addressed in part by prior work. The problem of efficient data collection in TWRI was first addressed in [10] and further developed in [11]–[13] through the use of compressive sensing (CS). In these works, an accurate image of a sparse scene of stationary targets was reconstructed using only a fraction of the original measurements. CS has been examined for moving targets in the context of TWRI in [14], showing similar advantages. A CS based method that reconstructs locations and Doppler of the targets in a two-step approach was proposed in [15]. However, none of these contributions has considered multipath propagation. Multipath exploitation in backprojection based radar imaging was first attempted in [16], wherein multipath returns were used to reveal information of hidden target areas, which were not in the line-of-sight of the radar. Following a similar idea, the work in [17] made use of the energy in the ghost targets resulting from secondary reflections at known interior walls to generate a ghost-free image with improved signal-to-clutter ratio (SCR). Multipath modeling and exploitation has further been considered as an inverse scattering problem in [18], [19]. Multipath exploitation within the CS framework was addressed in [20], [21] for sparsely-populated stationary indoor scenes. By using proper modeling under known wall locations, sparse reconstruction in this case yielded an image where ghosts were eliminated and their energy was added to the real targets.

In this paper, we bring CS based multipath exploitation to a general sparse indoor scene of stationary and moving targets. Assuming knowledge of the building layout, a forward linear multipath model based on ray-tracing for multistatic operation is developed, which is then used by a group sparse reconstruction approach for the underlying indoor scene. Our model is quite similar to the multi-input multi-output (MIMO) setup in [22], but cast in terms of multipath. We show that multipath propagation provides Doppler velocity diversity, which yields reconstruction benefits and improved velocity resolution capability. Furthermore, a two-step location and ve-

locity estimation method is proposed that extends the method of [15] to environments rich in multipath. In this scheme, subsequent to sparse reconstruction of the target locations, the Doppler information from different propagation paths is combined to obtain both crossrange and downrange velocity estimates with high accuracy. We demonstrate the effectiveness of the proposed multipath exploitation approaches through simulation and experimental results. In particular, we study the trade-off between computational complexity and reconstruction performance.

It is noted that moving target localization and velocity estimation can also be achieved through tracking. Tracking has been recently considered for TWRI applications in [23], wherein the targets are detected and their locations are tracked in consecutive images. However, motion or Doppler information in the measurements was not utilized in [23]. Tracking based methods should not be seen as alternatives to our proposed approach but rather as complementing each other. A tracking scheme would benefit from additional velocity estimates in each image. Conversely, the proposed CS-based approach does not take target dynamics into account and, thus, can benefit from a tracking method.

The remainder of the paper is organized as follows. In Section II, we introduce the multipath-free model for a wideband multistatic pulsed radar. Multipath propagation is incorporated in the model in Section III. In Section IV, the compressive sensing based image reconstruction method is proposed and the multipath-based target velocity estimation procedure is described. Subsequently, in Section V, we provide supporting simulation and experimental results. Finally, we conclude this paper in Section VI.

II. SIGNAL MODEL

In this section, we describe the signal model for a wideband multistatic pulsed radar system with M transmitters and N receivers located parallel to the x-axis. We consider a sequential sensing operation, i.e., only a single transmitter is active at a time and all N receivers are recording the returns. The model essentially follows [14].

Let the transmit signal be a modulated wideband pulse of duration T_p given by $\Re\{s(t)\exp(j2\pi f_c t)\}$, where t is the fast time, $s(t)$ is the pulse in the complex baseband, and f_c is the carrier frequency. We assume that the targets follow a translatory or linear motion with constant velocity in a two-dimensional (2D) space. Stationary targets are included as a special case of moving targets with zero velocity. Let K wideband pulses be transmitted by each transmitter with a pulse repetition interval (PRI) of T_r. The pulse index $k = 0, \ldots, K - 1$ is referred to as slow time. The PRI is assumed to be sufficiently small and the multiplexing of the transmitters sufficiently fast, such that i) the indoor scene can be considered approximately stationary during the sequential use of the M transmitters, i.e., over an interval of length MT_r, and ii) the movement of the indoor targets is approximately of constant velocity and slow enough so that the targets do not move out of a range cell during the observation interval of length KMT_r. Considering a scene of P point targets and

using the aforementioned assumptions, we can establish that the p-th target at pulse k is located at position

$$\boldsymbol{x}_p(k) = (x_p + v_{xp}kMT_r, y_p + v_{yp}kMT_r), \qquad (1)$$

where (x_p, y_p) is the target position at $t = 0$ and (v_{xp}, v_{yp}) is the target velocity vector. With the mth transmitter active, the emitted pulse travels through the wall to the target scene and the reflections are measured at the receive array. The baseband received signal corresponding to the mth transmitter, nth receiver, kth pulse, and pth target can be expressed as

$$\begin{aligned} z_{mnk}^p(t) = {} & \sigma_p s\left(t - kMT_r - mT_r - \tau_{pmn}(k)\right) \\ & \times \exp\left(-j2\pi f_c\left(kMT_r + mT_r + \tau_{pmn}(k)\right)\right), \end{aligned} \qquad (2)$$

where σ_p is the reflectivity of the pth point target and $\tau_{pmn}(k)$ is the bistatic two-way delay between the mth transmitter, pth target, and the nth receiver. In TWRI, as the transmitted waves are refracted twice at the front and back interfaces of the front wall and the backscattered wave is subject to the same double refraction before reaching the receiver, the delays can be computed using geometric considerations and Snell's law [24]. Assuming that the P targets do not interact with each other, the total baseband signal received by the nth receiver, corresponding to the kth pulse and the mth transmitter, is the superposition of all P target returns,

$$z_{mnk}(t) = \sum_{p=0}^{P-1} z_{mnk}^p(t). \qquad (3)$$

Note that the delays and the received signal generally depend on the slow time index k. However, if the velocity of the p-th target is zero, i.e., the stationary case, the delays do not change with k.

The measurements $\{z_{mnk}(t), m = 0, \ldots, M - 1, n = 0, \ldots, N - 1, k = 0, \ldots, K - 1\}$ can be discretized and vectorized to obtain a linear model of the system in matrix-vector form. The target space is assumed to be discretized into a grid with size $N_x \times N_y$ and similarly, the velocities are sampled on a discrete grid with size $N_{v_x} \times N_{v_y} = N_v$. In this 4D space, targets with any possible location or velocity are described by their reflectivities, whereas a non-existing target is represented by a zero reflectivity. Hence, in total, we have $N_x N_y N_v$ possible target states, which can be stacked into an $N_x N_y N_v \times 1$ vector $\boldsymbol{\sigma}$. The choice of the grid resolution is critical for sparse reconstruction. First, the computational complexity of the reconstruction scales with the number of grid points. Second, the density of the grid limits the accuracy of the location and velocity estimates. Third, the grid spacing determines the coherence of the dictionary matrix [25]. The latter yields a hard upper limit on the number of grid points as the reconstruction fails if the coherence is too high. A lower limit is reached when the grid is too coarse to accurately represent the targets, referred to as dictionary mismatch. Accuracy and computational complexity need to be traded off depending on the particular application and available resources. The received signal $z_{mnk}(t)$ is sampled uniformly at T time steps with sampling interval T_s. The sampling interval should be chosen to attain the Nyquist rate of the wideband

pulse $s(t)$. The samples can be stacked into a $T \times 1$ vector $\boldsymbol{z}_{mnk}$, which, using (1) and (2), can be expressed as

$$\boldsymbol{z}_{mnk} = \boldsymbol{\Psi}_{mnk} \boldsymbol{\sigma}, \tag{4}$$

where $\boldsymbol{\Psi}_{mnk}$ are the dictionary matrices obtained by discretizing the right hand side of (2), and are given by

$$[\boldsymbol{\Psi}_{mnk}]_{i,p} = s\left(t_i - kMT_r - mT_r - \tau_{pmn}(k)\right) \tag{5}$$
$$\times \exp\left(-j2\pi f_c\left(kMT_r + mT_r + \tau_{pmn}(k)\right)\right),$$
$$i = 0, \ldots, T-1, \quad p = 0, \ldots, N_x N_y N_v - 1.$$

Stacking of the received signal vectors $\boldsymbol{z}_{mnk}$ corresponding to all K pulses for all MN transmitter-receiver pairs results in a $TMNK \times 1$ measurement vector $\boldsymbol{z}$ as

$$\boldsymbol{z} = \boldsymbol{\Psi} \boldsymbol{\sigma}, \tag{6}$$

where $\boldsymbol{\Psi}$ is a $TMNK \times N_x N_y N_v$ dictionary matrix given by

$$\boldsymbol{\Psi} = \left[\boldsymbol{\Psi}_{0\,0\,0}^T \; \boldsymbol{\Psi}_{1\,0\,0}^T \; \cdots \; \boldsymbol{\Psi}_{M-1\,0\,0}^T \; \boldsymbol{\Psi}_{0\,1\,0}^T \; \cdots \right. \tag{7}$$
$$\left. \boldsymbol{\Psi}_{M-1\,N-1\,0}^T \; \boldsymbol{\Psi}_{0\,0\,1}^T \; \cdots \; \boldsymbol{\Psi}_{M-1\,N-1\,K-1}^T\right]^T.$$

Note that the linear model in (6) does not take multipath propagation into account. This will be treated in detail in Section III.

Besides multipath propagation, there is clutter caused by signal reflections from the front and interior walls. These type of returns originate from stationary building features and are not associated with indoor targets of interest. In realistic scenarios, the front wall radar returns can be very strong and may mask the behind-the-wall targets. As such, we incorporate the clutter returns in the received signal model. We consider two types of clutter, namely, wall returns and corner returns. The incident wave is reflected at any wall-air interface, for instance, at the front wall or a parallel interior wall, thereby causing wall returns. Further, any corner formed by two perpendicular walls acts as a dihedral reflector, resulting in corner returns. Since the walls and corners are stationary, the clutter does not change from pulse to pulse, i.e., it is invariant in the slow time domain.

Owing to their flat and smooth surfaces at the frequencies typically employed for TWRI, the walls reflect EM waves in a specular manner. As such, the signal propagates along a path with equal angles of incidence and reflection at the wall surface. Considering N_{w} exterior and interior walls, parallel to the array baseline, the wall returns can be described as

$$z_{kmn}^{\mathrm{wall}}(t) = \sum_{b=0}^{N_{\mathrm{w}}-1} \sigma_b^{\mathrm{wall}} s\left(t - kMT_r - mT_r - \tau_{bmn}^{\mathrm{wall}}\right) \tag{8}$$
$$\times \exp\left(-j2\pi f_c\left(kMT_r + mT_r + \tau_{bmn}^{\mathrm{wall}}\right)\right),$$

where σ_b^{wall} is the reflectivity of the bth wall and $\tau_{bmn}^{\mathrm{wall}}$ is the two-way propagation delay between the mth transmitter, the bth wall and the nth receiver. The delay is independent of the slow time index k and can be determined from the specular nature of the reflections and geometric considerations [14]. Additionally, the returns from N_{c} corners can be expressed as

$$z_{kmn}^{\mathrm{corner}}(t) = \sum_{u=0}^{N_{\mathrm{c}}-1} \sigma_{umn}^{\mathrm{corner}} s\left(t - kMT_r - mT_r - \tau_{umn}^{\mathrm{corner}}\right) \tag{9}$$
$$\times \exp\left(-j2\pi f_c\left(kMT_r + mT_r + \tau_{umn}^{\mathrm{corner}}\right)\right),$$

where $\sigma_{umn}^{\mathrm{corner}}$ is the reflectivity of the uth corner and $\tau_{umn}^{\mathrm{corner}}$ is the two-way propagation delay between the mth transmitter, the uth corner and the nth receiver. Note that, similar to the wall returns, the delay is independent of the slow time index k. However, the corner reflectivity depends on the transmitter and the receiver locations. The delay can be calculated in the same way as for point targets, while the reflectivity is given by [26]

$$\sigma_{umn}^{\mathrm{corner}} = \left(\frac{j2\sqrt{\pi}}{\lambda}\right)^{1/2} 2L_u$$
$$\times \mathrm{sinc}\left[\frac{4\pi L_u}{\lambda}\left(\cos(\psi_{um}^{\mathrm{t}} - \tilde{\psi}_u) - \cos(\psi_{un}^{\mathrm{r}} - \tilde{\psi}_u)\right)\right] \tag{10}$$
$$\times \begin{cases} \sin\left(\frac{\psi_{um}^{\mathrm{t}} + \psi_{un}^{\mathrm{r}} - 2\tilde{\psi}_u}{2}\right), & \psi_{un}^{\mathrm{r}}, \psi_{um}^{\mathrm{t}} \in [\tilde{\psi}_u, \tilde{\psi}_u + \frac{\pi}{4}] \\ \cos\left(\frac{\psi_{um}^{\mathrm{t}} + \psi_{un}^{\mathrm{r}} - 2\tilde{\psi}_u}{2}\right), & \psi_{un}^{\mathrm{r}}, \psi_{um}^{\mathrm{t}} \in [\tilde{\psi}_u + \frac{\pi}{4}, \tilde{\psi}_u + \frac{\pi}{2}], \end{cases}$$

where L_u is the length of the sides of the uth corner, $\tilde{\psi}_u$ is the orientation angle of the uth corner, $\psi_{um}^{\mathrm{t}}, \psi_{un}^{\mathrm{r}}$ are the respective angles of incidence and reflection, $\lambda = c/f_c$ is the wavelength, and c is the speed of light. Note that the angles are measured counterclockwise from the positive x-axis.

The overall radar return is, therefore, composed of target, wall, and corner returns and is given by

$$z_{kmn}^{\mathrm{total}}(t) = z_{kmn}(t) + z_{kmn}^{\mathrm{wall}}(t) + z_{kmn}^{\mathrm{corner}}(t), \tag{11}$$

which can be vectorized in the same fashion as described above for $z_{kmn}(t)$.

Due to the dominance of exterior wall clutter in TWRI, several wall mitigation techniques have been proposed in the literature. These include spatial filtering [27] and subspace projection [28] methods, which have been successfully applied in conjunction with compressive sensing and sparse scene reconstruction [10], [11], [29]. Both of these methods also remove the contributions of interior parallel walls as long as they are not shadowed by the contents of the building. In the sequel, we assume that the wall clutter has been properly mitigated. Further, we ignore the corner clutter and consider only the target returns for extending the received signal model to multipath propagation. However, in Section V, in addition to reconstruction examples based on target direct and multipath returns, we provide examples including the corner clutter to illustrate its effect on the performance of the proposed multipath exploitation scheme.

A. Conventional Image Formation

Conventional image formation for TWRI is carried out using backprojection or delay-and-sum beamforming (DSBF) [30], [31]. The complex image value $I_q(k)$, corresponding to the qth spatial grid point (x_q, y_q) and slow time index k, is obtained by summing delayed copies of the MN received signals corresponding to the kth pulse, followed by applying a matched filter with impulse response $s^*(-t)$ to the result, and then sampling the filtered data [31],

$$I_q(k) = \frac{1}{MN} \sum_{m=0}^{M-1} \sum_{n=0}^{N-1} z_{mnk}(t + \tau_{qmn}(k)) * s^*(-t)|_{t=0},$$
$$q = 0, 1, \ldots, N_x N_y - 1 \tag{12}$$

where τ_{qmn} is the focusing delay for the mth transmitter, nth receiver and the qth spatial grid point.

To obtain an overall image, $I_q(k), k = 0, 1, \ldots, K - 1$ cannot be simply combined coherently, as moving targets will be blurred and possibly mislocated. Instead, we can include the linear velocity model in the beamforming approach. We discretize the target space, as explained above, into a four-dimensional (4D) grid with two spatial and two velocity dimensions. Hence, we obtain an image value I_p at the pth space-velocity grid point $(x_p, y_p, v_{xp}, v_{yp})$ by a summation over the K pulses

$$I_p = \frac{1}{KMN} \sum_{k=0}^{K-1} \sum_{m=0}^{M-1} \sum_{n=0}^{N-1} z_{mnk}(t + \tau_{pmn}(k)) * s^*(-t)|_{t=0},$$
$$p = 0, 1, \ldots, N_x N_y N_v - 1 \tag{13}$$

where $\tau_{pmn}(k)$ is the focusing delay for the (m, n)th transmitter-receiver pair and the pth space-velocity grid point for the kth pulse. Thus, we obtain a set of 2D spatial images, each matched to a particular velocity vector. Equivalently, (13) can be obtained by taking the adjoint of (6)

$$\hat{\boldsymbol{\sigma}} = \boldsymbol{\Psi}^H \boldsymbol{z}, \tag{14}$$

where $\hat{\boldsymbol{\sigma}}$ contains vectorized spatial images corresponding to all considered velocities.

Note that the DSBF resolution is limited by the point spread function or Rayleigh resolution [32]. Further, DSBF provides severely degraded image quality in the case of missing or undersampled data. As such, sparse reconstruction is used for image formation from a few measurements. This will be detailed in the following sections and performance comparison with the velocity-matched beamforming will also be provided.

III. MULTIPATH PROPAGATION

Target multipath corresponds to indirect propagation paths, involving reflections at one or more secondary reflectors en route to the target of interest. Such secondary reflections can occur at interior walls, floor, and ceiling as well within the front wall. We only deal with interior wall multipath returns in this work. Floor/ceiling multipath is not considered as it is often weak, if not present, when using antennas with a narrow elevation beamwidth. We note, however, that this type of multipath can be treated in essentially the same manner as interior wall multipath. Multiple reflections within the front wall or wall ringing multipath has been treated in [20] for stationary scenes and can be similarly incorporated in this work.

The interior wall multipath returns can be classified into the following categories:

- *First order multipath*, which involves direct propagation to the target on transmit and one secondary reflection at

an interior wall on the way back to the receiver, or vice versa. This is the dominant case of multipath in TWRI.
- *Second order multipath*, wherein the signal undergoes two secondary reflections on the round-trip path to the target . Two cases can further be distinguished:
  - *Quasi-monostatic*, which involves one specular reflection on transmit and one on receive, both occurring at the same interior wall. Note that this corresponds to scattering at the target with a very small bistatic angle, as compared to first order multipath, when using a bistatic transmitter-receiver pair with a small baseline.
  - *Bistatic,* wherein the secondary reflections take place at two different walls. Both reflections can take place on transmit only, on receive only, or one on transmit and one on receive paths to the target.
- *Higher-order multipath*, which involves three or more secondary reflections during the round-trip path.

In the following, we will only consider the first two categories of interior wall multipath. As the signal is attenuated at each secondary wall reflection, the higher-order multipath returns are sufficiently weak to be safely neglected. Assuming that the quasi-monostatic reflection from indoor targets is stronger than bistatic scattering, we only take the quasi-monostatic second order multipath into consideration. As we are assuming perfect knowledge of the building layout, i.e., location, thickness, and permittivity of the front wall as well as the locations of the interior walls, we can accurately describe the multipath returns. In practice, exact prior knowledge of the room layout and wall properties may not be available. Hence, methods should be devised that take uncertainties in these parameters into account. A first step towards multipath exploitation under uncertainties in wall locations has been attempted in [33]. Using a ray tracing model, we will now calculate the exact delays corresponding to each considered path. The derivation follows essentially from [17], [20], [24].

A. Propagation Delays Due to Interior Wall Multipath

Interior wall multipath can be described by making use of the notion of a virtual target, as illustrated in Fig. 1, where the front wall has been ignored in the geometry for simplicity. We also do not explicitly state the dependence of the target location, propagation delay, and other associated parameters on the slow time index k in this section for simplicity of notation. The scene in Fig. 1 consists of a target located at $\boldsymbol{x}_p = (x_p, y_p)$ and an interior side wall, which is parallel to the y-axis and located at $x = w_1$. Now, consider propagation along the path $\mathcal{P}'$ from the target to a receiver via secondary reflection at the interior wall. Because of the specular nature of the interior wall reflection, a virtual target can be assumed to be present at the mirror image $\boldsymbol{x}_p' = (2w_1 - x_p, y_p)$ of the point $\boldsymbol{x}_p$. Then, the receive path $\mathcal{P}'$ involving the secondary reflection is equivalent to the direct path $\tilde{\mathcal{P}}'$ between the virtual target and the receiver. Hence, the calculation of the one-way propagation delay associated with path $\mathcal{P}'$ can be carried out by using the direct propagation path $\tilde{\mathcal{P}}'$. Note that the case of
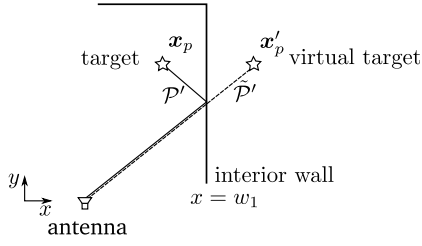
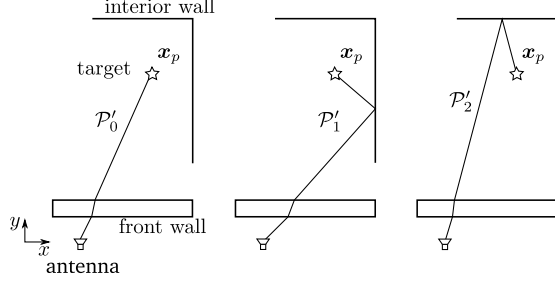Fig. 1. Multipath propagation via reflection at an internal wall.

Fig. 2. Example for three possible partial return paths.

the path from the transmitter to the target or reflection from a different wall can be treated in a similar manner.

With the mth transmitter active, the delay corresponding to the one-way path between receiver n and target p, is denoted by $\tau_{pmn}^{(\mathcal{P}')}$, which is equivalent to $\tau_{pmn}^{(\tilde{\mathcal{P}}')}$. When ignoring the front wall, the delay $\tau_{pmn}^{(\tilde{\mathcal{P}}')}$ can simply be calculated as the Euclidean distance between the receiver n and the virtual target at $\boldsymbol{x}_p'$ divided by the propagation speed. If the front wall is present, the double refraction at the front wall interfaces has to be taken into account, which can be accomplished using Snell's law [24]. It is noted that the same principle can be used for multipath via any interior wall.

B. Received Signal Model

Considering the aforementioned multipath mechanisms, we can formulate the model that describes the radar return under multipath propagation. To reiterate, the front wall response is not considered and we assume that the measurements contain only the target returns, as mentioned in Section II.

Any round-trip path $\mathcal{P}$ can be described as a combination of two one-way paths, namely, the path $\mathcal{P}''$ from the transmitter to the scattering target and the path $\mathcal{P}'$ from the target back to the receiver. Either of the two one-way paths can assume different forms, e.g., it could be the direct propagation to the target or involve a single reflection at an interior wall. We assume that there exist R_1 return paths between the target and the receiver, which will be denoted as $\mathcal{P}_{r_1}'$, $r_1 = 0, \ldots, R_1-1$. The same observation holds for the one-way transmit paths, which are denoted by $\mathcal{P}_{r_2}''$, $r_2 = 0, \ldots, R_2-1$. Therefore, there exist a total of $R_1 R_2$ round-trip paths. However, as mentioned earlier, we are only considering direct round-trip propagation and first-order and quasi-monostatic second-order multipath returns. As such, a maximum of $R < R_1 R_2$ combinations are considered for the round-trip path $\mathcal{P}$, i.e., $\mathcal{P}_r, r = 0, \ldots, R-1$. A function can be established that maps the index r of the round-trip path to a pair of indices of the one-way paths,
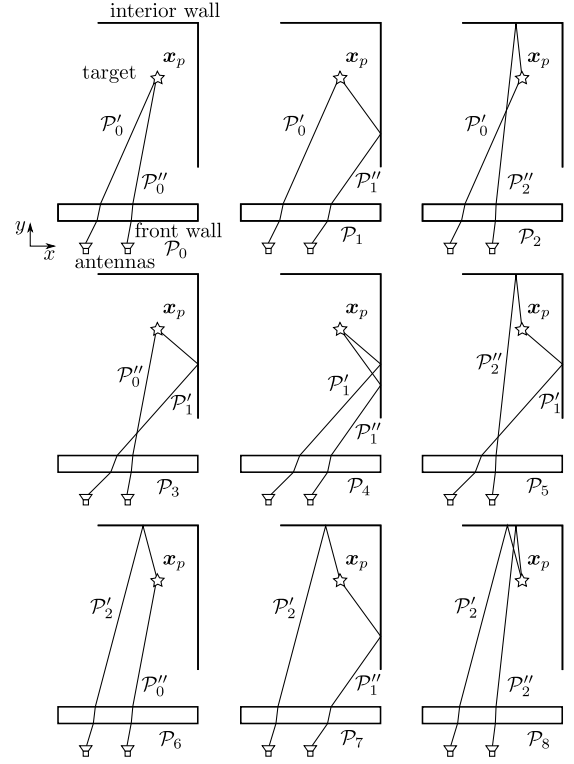

Fig. 3. Round-trip paths between transceiver and target for the partial paths shown in Fig. 2

$r \mapsto (r_1, r_2)$. In the following, we will consider $\mathcal{P}_0$ as the direct round-trip path, i.e., the case without any secondary reflections. This model is illustrated in Figure 2, which depicts three possible return paths, namely, direct propagation and secondary reflections from a side wall and the back wall. Three equivalent one-way paths will also be present for the propagation from the transmitter to the target. As a result, we obtain a total of nine round-trip paths, depicted in Figure 3, by combining three transmit paths and three return paths. Paths $\mathcal{P}_1, \mathcal{P}_2, \mathcal{P}_3$ and $\mathcal{P}_6$ correspond to first order multipath, $\mathcal{P}_4$ and $\mathcal{P}_8$ are quasi-monostatic second order multipath, while round-trip paths $\mathcal{P}_5$ and $\mathcal{P}_7$ are bistatic second order multipath. The latter are ignored in the model.

With the rth round-trip path $\mathcal{P}_r$ consisting of the one-way paths $\mathcal{P}_{r_1}'$ and $\mathcal{P}_{r_2}''$, the corresponding round-trip delay $\tau_{pmn}^{(r)}$ between the mth transmitter, nth receiver, and p-th target can be expressed as

$$\tau_{pmn}^{(r)} = \tau_{pmn}^{\mathcal{P}_{r_1}'} + \tau_{pmn}^{\mathcal{P}_{r_2}''}. \tag{15}$$

where the one-way path delays $\tau_{pmn}^{\mathcal{P}_{r_1}'}$ and $\tau_{pmn}^{\mathcal{P}_{r_2}''}$ can be computed using the method described in Section III-A.

Further, at each reflection and refraction along the rth round-trip path, the traveling wave will undergo some attenuation and possibly a phase shift, which is captured by the associated complex amplitude $\Gamma_{pmn}^{(r)}$. The complex amplitudes for the R paths depend on the dielectric properties of the front and interior walls and the corresponding angles of incidence and refraction. A detailed derivation can be found in [17], [20]. Assuming that the transmit and receive arrays are co-located and have sufficiently small extents as compared to the distance

to the scene, the incident, refraction, and reflection angles associated with a particular path do not vary much across the arrays. As such, the dependence of $\Gamma_{pmn}^{(r)}$ on transmitter m and receiver n can be ignored, i.e., $\Gamma_{pmn}^{(r)} \approx \Gamma_p^{(r)}$. Additionally, as the direct round-trip path return from a target is typically the strongest path compared to the associated multipath, the corresponding complex amplitudes are normalized w.r.t. the direct path in order to avoid over-parameterization,

$$g_p^{(r)} = \frac{\Gamma_p^{(r)}}{\Gamma_p^{(0)}}, \quad r = 0, \ldots, R-1, \quad p = 0, \ldots, N_x N_y N_v - 1. \tag{16}$$

Hence, we assign a single complex path weight $g_p^{(r)}$ to the rth possible path corresponding to the pth target state and a transmitter/receiver combination, with the direct path having the weight $g_p^{(0)} = 1$.

We are now in a position to formulate the target signal model under multipath propagation. The received signal is expressed as a superposition of delayed and weighted versions of the transmitted signal corresponding to all possible propagation paths $r = 0, \ldots, R-1$. That is,

$$\boldsymbol{z} = \boldsymbol{\Psi}^{(0)}\boldsymbol{\sigma}^{(0)} + \boldsymbol{G}^{(1)}\boldsymbol{\Psi}^{(1)}\bar{\boldsymbol{\sigma}}^{(1)} + \cdots + \boldsymbol{\Psi}^{(R-1)}\boldsymbol{G}^{(R-1)}\bar{\boldsymbol{\sigma}}^{(R-1)}, \tag{17}$$

where $\boldsymbol{G}^{(r)} = \mathrm{diag}(g_0^{(r)}, g_1^{(r)}, \ldots, g_{N_x N_y N_v - 1}^{(r)}), r = 0, \ldots, R-1$ are the path weight matrices, and the dictionaries $\boldsymbol{\Psi}^{(r)}, r = 0, \ldots, R-1$ are defined according to (5) and (7) with τ_{pmn} replaced by $\tau_{pmn}^{(r)}$. Note that, in (17), we assume an individual target state vector $\bar{\boldsymbol{\sigma}}^{(\cdot)}$ for each path, as the phase and amplitude of the target reflectivity change in general with the bistatic angle and target orientation. Further, we assume the same number of paths for each target state, as a particular path weight can be set to zero if the corresponding path is not available for that target state.

For notational convenience, the path weights can be absorbed into the target state vectors as $\boldsymbol{\sigma}^{(r)} = \boldsymbol{G}^{(r)}\bar{\boldsymbol{\sigma}}^{(r)}$, as the weighting imposes only a per target state scaling. The resulting linear measurement model takes the form

$$\boldsymbol{z} = \boldsymbol{\Psi}^{(0)}\boldsymbol{\sigma}^{(0)} + \boldsymbol{\Psi}^{(1)}\boldsymbol{\sigma}^{(1)} + \cdots + \boldsymbol{\Psi}^{(R-1)}\boldsymbol{\sigma}^{(R-1)}. \tag{18}$$

Note that (18) is a generalization of the single path propagation model in (6). If the number of propagation paths is set to 1, then the two models are equivalent. Further note that the measurement model (18) does not make any assumptions about the resolvability of the various multipath arrivals. If the multipath returns are resolvable and successful association can be made between each signal component and its respective propagation path, the model would be similar to multipath-free widely-separated MIMO operation as used in [34]. Since resolving and associating multipath components is difficult in practice, we employ the additive model (18).

C. Apparent Doppler Velocity

In order to study the effect of multipath and motivate its exploitation, we examine the information contained in the multipath returns [35]. A target at initial position (x_p, y_p) moving with uniform velocity (v_{xp}, v_{yp}) has different apparent Doppler velocities when observed via different propagation
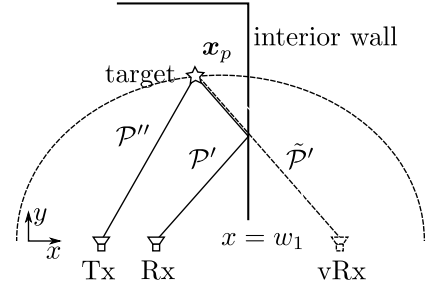

Fig. 4. Alternate multipath geometry with a virtual receiver and the corresponding constant range ellipse.

paths. In case of direct propagation and a monostatic setup, this is the radial velocity component with respect to the location of the transceiver. Intuitively, in a monostatic radar, the locus of equal range is a circle which is also the trajectory of zero Doppler. Thus, only velocities perpendicular to this circle, i.e., radial velocities, can be observed. For a bistatic setup, the trajectory of zero Doppler velocity forms an ellipse with the interrogating transmitter/receiver pair as foci and the observable velocity component is the normal to this ellipse.

If the transmitted pulse travels along an indirect path, the apparent Doppler velocity changes. In order to determine the form of the apparent Doppler velocity under multipath propagation, we consider an alternate transmitter/receiver/target geometry for the multipath by reflecting the physical transmitter and/or receiver locations about the secondary reflector (interior wall). For first order multipath, either the transmitter or receiver location is mirrored depending on whether the secondary reflection occurrs on transmit or receive. On the other hand, both the transmitter and receiver locations will be mirrored for second order quasi-monostatic multipath propagation. The mirrored locations constitute a virtual transmitter and a virtual receiver. We can now cast the multipath as direct propagation to/from these virtual antenna locations. As such, for apparent Doppler velocity corresponding to multipath propagation, the normal velocity component with respect to the ellipse formed by the virtual transmitter/receiver is a relevant measure. Hence, the observed Doppler velocity of the target under multipath propagation is the projection of the target velocity onto this normal. An example scenario is depicted in Fig. 4, where multipath occurs on the return path only. The signal travels along path $\mathcal{P}''$ from the physical transmitter (Tx) to the target and along path $\mathcal{P}'$ back to the physical receiver (Rx) via reflection at the interior wall. The return path can equivalently be described by direct propagation along path $\tilde{\mathcal{P}}'$ to a virtual receiver (vRx) that has been constructed as described above. Now, the normal to the ellipse formed by the physical transmitter (Tx) and the virtual receiver (vRx) needs to be considered for the apparent Doppler velocity. This velocity may also be approximated using propagation delays. Depending on the transmitter m, the receiver n, the path r, and averaging over the full CPI, the apparent Doppler velocity for the pth target may be expressed as

$$v_{D,pmn}^{(r)} = \frac{1}{K-1} \sum_{k=0}^{K-2} c \frac{\tau_{pmn}^{(r)}(k+1) - \tau_{pmn}^{(r)}(k)}{T_r}. \tag{19}$$
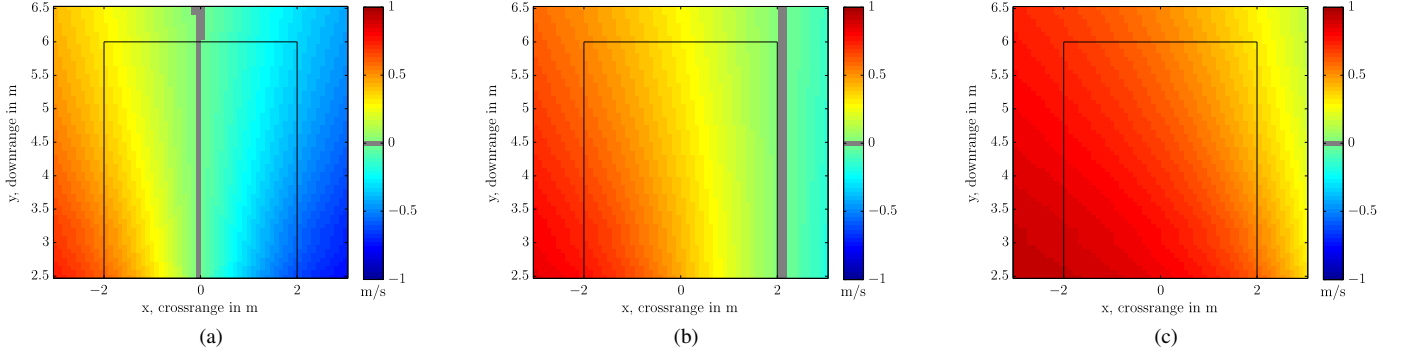
Fig. 5. Apparent Doppler velocity for a target moving with velocity $(1,0)$m/s for (a) the direct path, (b) first order multipath via right side wall, and (c) second order multipath via right side wall.

Hence, for each target, we obtain R apparent Doppler velocities, which are the projections of the target velocity vector on the respective normal directions. These will be exploited to obtain an estimate of the full target velocity vector. Note that for sufficiently small arrays, the apparent Doppler velocity does not change with the transmit/receive array elements and, hence, only depends on the propagation path as well as the target location and velocity.

For illustration, we simulate a target at an arbitrary location within three walls, moving with a velocity $(v_{xp}, v_{yp}) = (1, 0)$ m/s. That is, the target is solely moving in the crossrange direction. At each assumed target position, the apparent Doppler velocity is color coded in Fig. 5. The surrounding walls are also superimposed on the figure. The velocity pattern is only shown for a single transmitter/receiver pair located at the centers of the transmit and receive arrays. In the direct propagation case, shown in Fig. 5a, we observe the expected pattern, with zero velocity along broadside and gradually increasing velocity for angles deviating from broadside. However, the pattern is different for indirect paths, reaching the target via reflection at the right side wall, as shown in Figs. 5b,c. Fig. 5b corresponds to a first order multipath that involves direct propagation on transmit and a secondary reflection at the right side wall on receive, whereas Fig. 5c involves a secondary reflection at the right side wall on both transmit and receive. The patterns in Figs. 5b,c are shifted and distorted as compared to Fig. 5a. In particular, the zero velocity line is shifted as compared to that in Fig. 5a. Hence, we obtain additional information on target motion through the first and second order multipath returns. If properly modeled, as described earlier, this property is exploited to improve the velocity estimation.

IV. COMPRESSIVE SENSING BASED SCENE RECONSTRUCTION

Benefits of CS are realized when the radar return is undersampled in all four dimensions, i.e., fast time, slow time and transmit/receive elements. For the latter two, most savings are achieved by random omission of some elements, leading to sparse transmit and receive arrays. Random undersampling of slow time does not lead to any benefits in terms of time or cost savings, as long as the first and the last pulses are retained in the CPI. However, reducing the number of pulses

within the CPI leads to power savings, which may be desirable in portable applications. Various methods are available to compressively sample in the fast time. Here, we adopt a random mixing scheme in which each pulse is correlated with a set of random signals and only the corresponding correlation result is sampled. For a detailed discussion of this scheme, the reader is referred to [14], [36].

The compressively sampled version of the radar return in (18) can be expressed as

$$\bar{z} = \Phi z = \Phi(\Psi^{(0)}\sigma^{(0)} + \Psi^{(1)}\sigma^{(1)} + \cdots + \Psi^{(R-1)}\sigma^{(R-1)}), \tag{20}$$

where J is the number of reduced measurements, and the measurement matrix $\Phi \in \mathbb{R}^{J \times TMNK}$ represents the under-sampling operation. With the aforementioned undersampling considerations, reducing the number of samples along transmit elements to M_d, along receive elements to N_d, along slow time to K_d, and along fast time to T_d, is achieved by a measurement matrix constructed as [14]

$$\begin{aligned} \Phi = &(\Phi_1 \otimes I_{N_d K_d T_d}) \cdot (\Phi_2 \otimes I_{MK_d T_d}) \cdot (\Phi_3 \otimes I_{MNT_d}) \\ &\cdot \mathrm{diag}(\Phi_4^{(0)}, \dots, \Phi_4^{(MNK-1)}), \end{aligned} \tag{21}$$

where $\otimes$ denotes Kronecker product and I_a is an identity matrix of dimension a. The total number of reduced measurements is given by $J = T_d M_d N_d K_d \ll TMNK$. Each of the matrices $\Phi_1 \in \mathbb{R}^{M_d \times M}$, $\Phi_2 \in \mathbb{R}^{N_d \times N}$ and $\Phi_3 \in \mathbb{R}^{K_d \times K}$ consists of randomly chosen rows from an identity matrix, while random mixing in fast time is achieved by Gaussian random matrices $\Phi_4^{(i)} \in \mathbb{R}^{T_d \times T}$ with entries drawn form a standard normal distribution. Other random matrices, e.g., drawn from a Bernoulli distribution, can also be considered to achieve a good trade-off between ease of implementation and performance, see [36].

A. Group Sparse Scene Reconstruction With Joint Velocity Estimation

In order to account for all propagation paths, a high-dimensional model is constructed using (20) as

$$\bar{z} = \Phi \tilde{\Psi} \tilde{\sigma} \tag{22}$$

where $\tilde{\Psi} = [\Psi^{(0)} \ \Psi^{(1)} \ \cdots \ \Psi^{(R-1)}] \in \mathbb{C}^{MNKT \times N_x N_y N_v R}$ is the concatenated overcomplete dictionary for all possible

paths and the unknown target state vectors are stacked into a single tall vector

$$\tilde{\boldsymbol{\sigma}} = \left[\left(\boldsymbol{\sigma}^{(0)}\right)^T \; \left(\boldsymbol{\sigma}^{(1)}\right)^T \; \cdots \; \left(\boldsymbol{\sigma}^{(R-1)}\right)^T \right]^T. \qquad (23)$$

Given the reduced measurements $\bar{\boldsymbol{z}}$ in (22), we aim at recovering the target state information $\tilde{\boldsymbol{\sigma}}$ using sparse reconstruction. If no multipath propagation is present, this can be achieved by standard ℓ_1-norm minimization, as considered in [14]. However, this method is suboptimal in the presence of multipath. Similar to [20], we exploit multipath by utilizing the group sparse structure in the target state information. More specifically, the target state vectors corresponding to each path exhibit a group sparse structure, where the individual groups extend across the paths for each target state. Note that the apparent Doppler velocity for a particular target may differ when observed through different paths. This is captured in the model through different delays $\tau_{pmn}^{(r)}(k)$, which are a function of slow time and are all calculated based on the same coordinate system. In this way, the reconstruction benefits from the additional diversity in the received signal due to different Doppler velocities corresponding to the same target.

The group sparse reconstruction of the unknown vector $\boldsymbol{\sigma}$ is achieved by solving the mixed ℓ_2/ℓ_1-norm minimization problem

$$\hat{\boldsymbol{\sigma}} = \arg\min_{\tilde{\boldsymbol{\sigma}}} \|\bar{\boldsymbol{z}} - \boldsymbol{\Phi}\tilde{\boldsymbol{\Psi}}\tilde{\boldsymbol{\sigma}}\|_2^2 + \mu\|\tilde{\boldsymbol{\sigma}}\|_{1,2}, \qquad (24)$$

where

$$\|\tilde{\boldsymbol{\sigma}}\|_{1,2} = \sum_{p=0}^{N_x N_y N_v - 1} \left\| \left[\sigma_p^{(0)}, \sigma_p^{(1)}, \ldots, \sigma_p^{(R-1)}\right]^T \right\|_2 \qquad (25)$$

and μ is a regularization parameter. The convex optimization problem (24) can be solved using SparSA [37], BOMP [38], or other available schemes [39], [40]. In the sequel, we contrast the optimization based approach SparSA and the greedy method BOMP. SparSA obtains a near-optimum solution for (24) at the cost of high numerical complexity, whereas the BOMP finds a sub-optimal solution at significantly lower computational cost.

Once a solution $\hat{\boldsymbol{\sigma}}$ is obtained, a composite target state vector corresponding to the scene can be obtained by non-coherent combination of the state vectors corresponding to the various paths as

$$[\hat{\boldsymbol{\sigma}}_{\text{comb}}]_p = \left\| \left[\sigma_p^{(0)}, \sigma_p^{(1)}, \ldots, \sigma_p^{(R-1)}\right]^T \right\|_2, \qquad (26)$$

where $p = 0, \ldots, N_x N_y N_v - 1$. The final recovery result contains the information about the location and the translatory motion of all targets in the scene. Stationary targets are included in the spatial image corresponding to the zero velocity case. For an in-depth treatment of the group-sparse reconstruction approach, the reader is referred to [20].

Note, that the model (22) and the reconstruction problem (24) apply to a wide range of TWRI sensor configurations. For example, for highly aspect-dependent targets, the arrays can be split into multiple sub-arrays and multiple models of the form (22) are stacked vertically to accommodate the new set of measurements and corresponding images. In this case, the groups extend over all paths and sub-arrays. Similarly, one can deal with frequency-dependent targets by splitting the pulse into various sub-pulses covering only parts of the full bandwidth and adjusting the model in the same fashion as described above. These extensions come at the cost of higher computational complexity and degraded reconstruction performance as a much larger number of unknowns has to be recovered. However, they provide additional flexibility for challenging radar deployment/logistics or target types.

B. Group Sparse Scene Reconstruction With Subsequent Velocity Estimation

We further propose a two-step method that first estimates the target locations based on compressive sensing and subsequently performs velocity estimation using conventional Doppler processing. In so doing, we extend the approach by Dang and Kilic [15] to account for and exploit multipath propagation. Instead of reconstructing the full 4D target state vector as in (24), we solve a 2D reconstruction problem for each slow time index individually. As the returns at a single slow time do not contain any velocity information, only the spatial information of the scene is reconstructed. For each $\check{z}(k)$, a scene reflectivity vector $\hat{\boldsymbol{\sigma}}^{(r)}(k)$ is reconstructed by solving

$$\hat{\boldsymbol{\sigma}}^{(r)}(k) = \arg\min_{\boldsymbol{\sigma}^{(r)}(k), r=0,\ldots,R-1} \|\check{z}(k) - \sum_{r=0}^{R-1} \check{\boldsymbol{\Phi}}\check{\boldsymbol{\Psi}}^{(r)}\boldsymbol{\sigma}^{(r)}(k)\|_2^2$$
$$+ \mu \sum_{p=0}^{N_x N_y - 1} \left\| \left[\sigma_p^{(0)}(k), \sigma_p^{(1)}(k), \ldots, \sigma_p^{(R-1)}(k)\right]^T \right\|_2, \quad (27)$$

where $k = 0, \ldots, K - 1$. The downsampling matrix $\check{\boldsymbol{\Phi}} \in \mathbb{R}^{T_d M_d N_d \times TMN}$ is constructed in the same manner as described above. However, no downsampling in the slow time domain is performed. The measurement vectors are formed by stacking the returns corresponding to all transmitters and receivers for each pulse as $\boldsymbol{z}(k) = [\boldsymbol{z}_{0\ 0\ k}^T, \ldots, \boldsymbol{z}_{M-1\ N-1\ k}^T]^T, k = 0, \ldots, K - 1$ and $\check{z}(k) = \check{\boldsymbol{\Phi}}\boldsymbol{z}(k)$. The reduced dictionaries $\check{\boldsymbol{\Psi}}^{(r)} \in \mathbb{R}^{MNT \times N_x N_y}$ are part of the full dictionaries $\boldsymbol{\Psi}^{(r)}$ corresponding to $k = 0$ and zero target velocity. Note that despite solving K different CS problems, the corresponding computational load is much lower as the number of unknowns is greatly reduced (by the potentially large number of velocity bins N_v). An intermediate image containing target location reconstruction can then be formed by a non-coherent summation over all paths and pulses. At this point, a target detection step should be carried out to select only N_p targets with significant amplitude to maintain the computational complexity at a manageable level in the subsequent velocity estimation procedure.

In step 2 of the method, the velocity vector for each target is estimated by further processing of the sparse scene reconstruction result. For each of the N_p targets, we obtain KR complex values, one for every combination of propagation path and pulse, denoted by $\boldsymbol{b}_p^{(r)} = [\hat{\sigma}_p^{(r)}(0), \ldots, \hat{\sigma}_p^{(r)}(K-1)]^T \in \mathbb{C}^K, p = 0, \ldots, N_p - 1, r = 0, \ldots, R - 1$. The apparent

Doppler velocity of the target causes a phase progression along the slow time dimension k. The amount of phase progression per pulse encodes the Doppler velocity and depends on the location/velocity of the target as well as the propagation path. We take the discrete-time Fourier transform of $\boldsymbol{b}_p^{(r)}$ along the slow time to obtain the Doppler information $B_p^{(r)}(\omega)$ for the detected targets. Assuming only a single target per location cell, we can determine the apparent Doppler velocities for each target and path by finding the peaks in the Fourier-transformed slow time vectors. Hence, for each target, we obtain R apparent Doppler velocities

$$v_{D,p}^{(r)} = \frac{c}{\pi f_c} \arg\max_\omega B_p^{(r)}(\omega) \qquad (28)$$

that correspond to the projections onto the normal velocity vectors as discussed in Section III-C. Finally, we can express the linear relationship between the target velocity vectors and the Doppler velocities as

$$\left[v_{D,p}^{(0)}, \ldots, v_{D,p}^{(R-1)}\right]^T = \boldsymbol{V}_p \begin{bmatrix} v_{px} \\ v_{py} \end{bmatrix}, p = 0, \ldots, N_p - 1, \quad (29)$$

where the rows of $\boldsymbol{V}_p$ contain the normal velocities for each path at the location of the pth target. The over-determined linear equation system (29) can be solved using a least squares approach to obtain a velocity estimate $(v_{px}, v_{py})^T$. Note that the exploitation of multipath enables an estimate of the full target velocity vector, whereas a single path may only deliver a scalar Doppler speed.

The described velocity estimation method can be extended to multiple targets within a single location resolution cell. In this case, multiple apparent Doppler velocities need to be extracted from each path. This, however, results in resolution and target association issues. First, multiple Doppler velocities may only be determined provided that they are sufficiently distinct and can be resolved in the Fourier-transformed slow time. Second, the association of the found velocities to the targets is not obvious. In the case of a few targets per cell and a few paths, a combinatorial search may be feasible. That is, every possible association is attempted and the result with the lowest estimation residual is chosen to be the correct velocity estimate. The final result of this two-step method is a reconstructed image of the scene and corresponding velocity estimates for the detected targets.

Note that despite involving K different sparse reconstruction problems, the two-step approach has a much lower computational load compared to the sparsity-based joint location and velocity estimation approach. Typical sparse reconstruction schemes have at least linear complexity in the number of unknowns [37]. As such, the complexity of the joint estimation approach is $\mathcal{O}(N_x N_y N_v R)$, while that for solving K sparse reconstruction problems in the two-step approach is $\mathcal{O}(K N_x N_y R)$. Further, the computational load of the least-squares step in the latter approach is negligible. Hence, an overall reduction of complexity by a factor N_v / K is achieved for the two-step approach. This is supported by empirical results of the computational complexity as discussed in the following section.
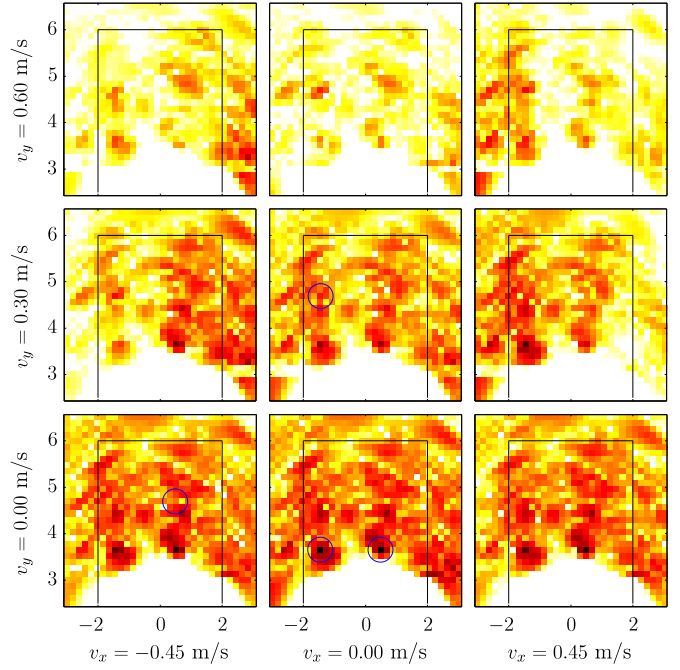

Fig. 6. Delay and sum beamforming result using full data.

V. RESULTS

We present simulation and experimental results to deomstrate the effectiveness of the proposed multipath exploitation approaches. The setups are chosen such that they represent a realistic wideband pulsed TWRI system. The multipath environment is modeled to mimic a typical room behind a concrete exterior wall. In all simulation examples, independent and identically distributed complex circular Gaussian receiver noise with a signal-to-noise ratio of 10 dB is added to the measurements before applying the downsampling operation. All reconstruction results are shown on a 60 dB scale.

A. Simulation Results

Simulations were performed for a wideband pulse-Doppler multistatic radar with a 4-element uniform linear array of length 1 m. Each array element can be used for both transmission and reception, leading to $M = N = 4$. A modulated Gaussian pulse, centered around $f_c = 2$ GHz, with a relative bandwidth of 50% is transmitted. The PRI is set to 10 ms and $K = 15$ pulses are processed coherently. At the receiving side, $T = 150$ fast time samples in the relevant interval, covering the target and multipath returns, are taken at a sampling rate of $f_s = 4$ GHz. The front wall is modeled with $d = 20$ cm thickness and relative permittivity $\epsilon_r = 7.66$, and is located parallel to the array at a distance of 3 m. Two side walls are considered at ± 2 m in crossrange, each of which causes 3 different multipath returns per target. There are, in total, four first order multipath returns and two second order quasi-monostatic multipath returns per target, which are all considered to be 6 dB weaker than the direct path. Hence, in total, there are $R = 7$ paths per target contributing to the received signal. We assume that the returns from the front wall have been properly suppressed. We neither consider any

wall returns nor any multipath from the back wall located at 6 m downrange. Stationary clutter, if included, would be reconstructed as part of the zero-velocity spatial image. If the depiction of stationary targets and clutter is not desired, either a simple moving target indicator method can be employed or the reconstructed targets with zero velocity can be masked out in the final image. For the two-step method, a threshold for minimum speed of interest should be set to avoid reconstructions of the stationary targets and clutter. The imaged region extends 6 m in crossrange and 4 m in downrange and is centered at a point 4 m in downrange along the broadside direction of the array. The scene is spatially discretized into an $N_x \times N_y = 32 \times 32$ pixel grid. The target velocities are discretized on an $N_{v_x} \times N_{v_y} = 5 \times 7$ grid, spanning target velocity components ranging from -0.9 m/s to 0.9 m/s.

1) Imaging Results: We consider two stationary targets residing at spatial coordinates $(0.5, 3.7)$ m and $(-1.5, 3.7)$ m and two moving targets at $(0.5, 4.7)$ m and $(-1.5, 4.7)$ m, respectively. The moving targets are assumed to be 8 dB weaker than the stationary targets and possess respective velocities $(-0.45, 0)$ m/s and $(0, 0.3)$ m/s. At first, no returns from the room corners are considered. We assume that all targets are visible via all $R = 7$ possible paths. We first show the conventional beamforming results using full measurements in Fig. 6, where the beamformer for each spatial image has been matched to the corresponding velocity pair according to (14). The resulting image appears very cluttered due to the multipath responses and the moving targets cannot be discerned. We present in Fig. 7 the multipath exploitation based sparse reconstruction using 7% of the full Nyquist sampled measurements, averaged over 20 Monte Carlo runs. The downsampling parameters of (21) are set to $T_\mathrm{d} = 20$, $M_\mathrm{d} N_\mathrm{d} = 8$ and $K_\mathrm{d} = 15$, performing linear measurements using a Gaussian random mixing matrix in fast time. The selection of the downsampling parameters is constrained by three factors. First, the coherence of the dictionary determines the performance of the reconstruction algorithms. Second, the assumed sparsity of the scene yields a lower limit on the reduced number of measurements. Third, the SNR of the received signal affects the CS result. Due to noise folding, the effective SNR in the measurements decreases for decreased T_d [41]. Therefore, the selection of the downsampling factor in the fast time must be cognizant of the noise level.

We contrast three different algorithms: group sparse CS (GSCS) with joint location and velocity estimation using a) an optimization-based approach (SparSA) and b) a greedy approach (BOMP); c) the two-step approach with SparSA in the location reconstruction and least-squares method for velocity estimation. The regularization parameter in the SparSA reconstruction is set to $\mu = \mu_\mathrm{norm} \|(\boldsymbol{\Phi}\tilde{\boldsymbol{\Psi}})^H \check{\boldsymbol{z}}\|_\infty$, with $\mu_\mathrm{norm} = 0.1$. Note that the optimal choice of the regularization parameter μ is still an open problem and has not been considered in this work. For the BOMP, we assume a sparsity level of 20 nonzero groups which is an overestimate of the true sparsity level. In each case, a composite image is shown, where the magnitudes are accumulated over velocities for the group sparse methods and over the slow time for the two step approach. The velocity estimates for the four strongest targets are indicated

on the spatial scene reconstructions using arrows. The group sparse reconstruction using SparSA, shown in Fig. 7, features perfect reconstruction of the target positions and velocities. The ghost targets have been suppressed and only a few very weak clutter pixels remain. Greedy reconstruction using the BOMP also successfully locates the targets and determines their velocities, but exhibits strong clutter along the side walls, as depicted in Fig. 7b. As the BOMP is a greedy method, a locally optimal choice of an image pixel is performed in each iteration. Locations along the side wall are special in the sense that four propagation paths coincide, namely, the direct path and the three indirect paths via the respective wall. The almost perfect correlation of the corresponding dictionary elements may lead to a false selection in the BOMP. The result of the two-step approach is provided in Fig. 7c, which generally shows larger background noise and lower signal-to-clutter ratio. The four targets and the corresponding velocities are accurately reconstructed nonetheless. To evaluate the numerical complexity, we compare the average runtime of the following three algorithms: joint estimation using SparSA, joint estimation using BOMP, and the two-step approach with SparSA employed in the first step. A single core of a 2.8 GHz CPU was used for the calculations. The average runtime of the joint estimation using SparSA was 170.3 min, while those for joint estimation using BOMP and the two-step approach were 11.1 min and 5 min, respectively. Both BOMP-based joint estimation and the two-step method are one order of magnitude faster than the joint estimation using SparSA, with the two-step approach being the fastest due to its much reduced CS problem size.

Next, the impact of the corner returns on the performance of the proposed schemes is evaluated. The above simulation is repeated with the returns from the two corners in the back of the room included in the received signal. The corner returns are modeled according to (9) with $N_\mathrm{c} = 2$ and $L_u = 2$ m, $u = 0, 1$. The averaged images along with velocity estimates for the 50 strongest targets are presented in Fig. 8. The CS multipath exploitation result using SparSA is shown in Fig. 8a. The target locations and velocities are depicted correctly, but strong clutter is now visible at the two considered corners of the room. Since the corner reflectivity varies across the various transmitter-receiver pairs, the imaged corners are smeared in space and velocity. Similar results are achieved using the BOMP, see Fig. 8b. However, the clutter along the side walls is more pronounced and the relative amplitude of the targets is weak. Finally, the imaging result of the two-step approach in Fig. 8c is similar to the SparSA reconstruction, but the velocity reconstruction for the two moving targets fails. Also, the velocity estimates for the stationary corner reflections are significantly off.

2) Velocity estimation: We carry out another simulation which specifically focuses on velocity estimation. First, we show that the additional information on the target velocity contained in the multipath returns can be exploited to improve the velocity resolution. We employ the proposed CS reconstruction scheme from Sec. IV-A using SparSA to resolve two targets with similar velocities. The targets are fixed at 4 m downrange in the broadside direction of the array, while the room and
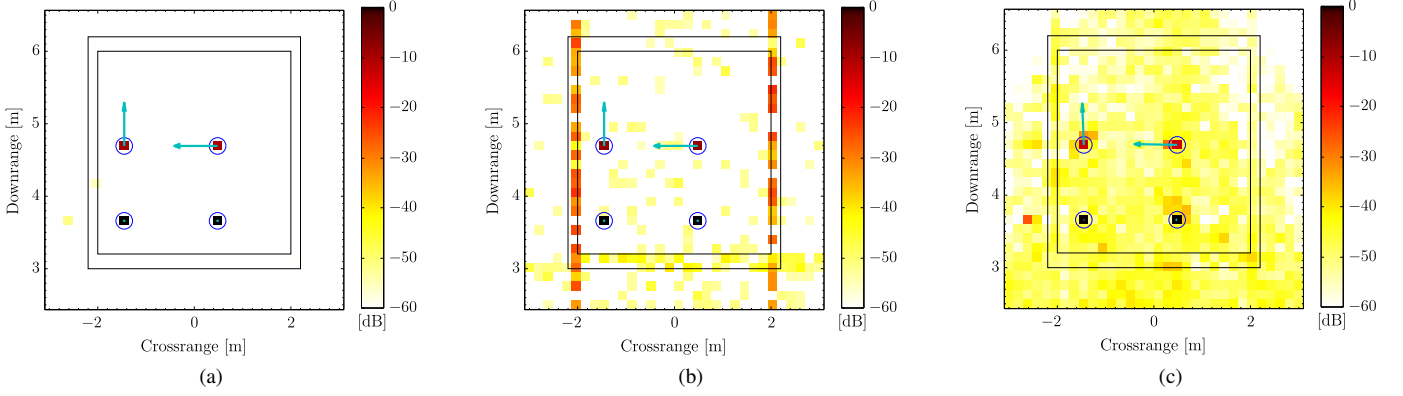
Fig. 7. CS reconstruction using 7% of the measurements for (a) GSCS using SparSA, (b) GSCS using BOMP, and (c) the two-step approach.
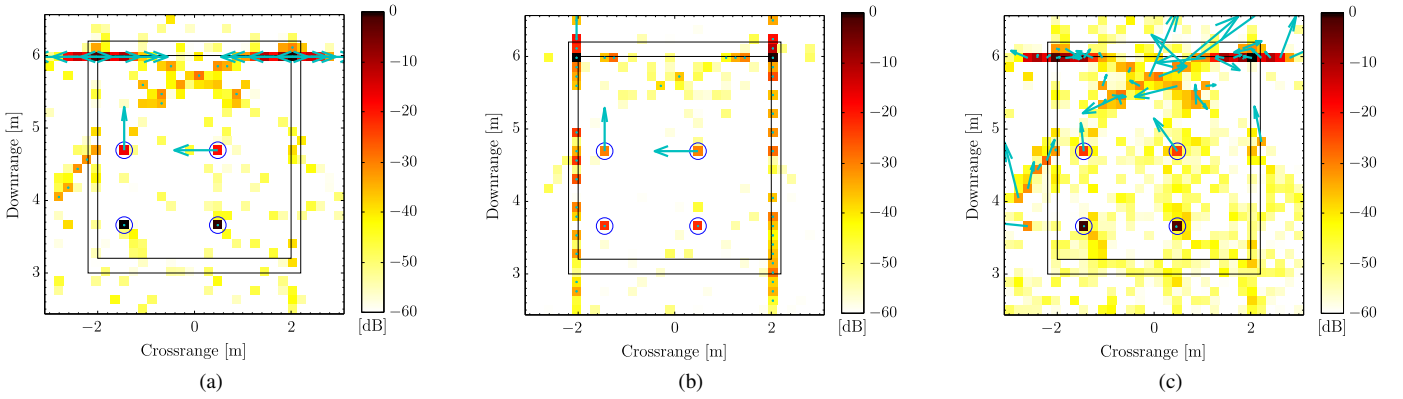

Fig. 8. CS reconstruction including corner using 7% of the measurements for (a) GSCS using SparSA, (b) GSCS using BOMP, and (c) the two-step approach.

system parameters are kept the same as in the previous examples. Both targets reside in the same range/crossrange cell, but move in opposing crossrange directions. The target velocities differ by only 0.8 m/s. The 11×11 velocity grid covers range/crossrange velocities between ± 1 m/s. We present the results in Fig. 9 for exploiting different numbers of multipath returns: i) the direct propagation path only ($R = 1$), ii) direct and first order multipath returns only ($R = 5$), iii) a second order multipath in addition to the direct and first order multipath returns ($R = 6$), and iv) all seven paths per target as described above. It is evident that the velocity resolution capability improves with the incorporation of an increasing number of multipath returns. If only the direct path is available, the two moving targets cannot be resolved, as seen in Fig. 9a. If all four first order multipath returns are included and exploited, the two targets are resolved, but neighboring clutter pixels may render the velocity estimation difficult, see Fig. 9b. Finally, when either six or seven paths are available and exploited, the two moving targets are resolved with accurate velocity estimates, as evident in Figs. 9c,d.

In order to compare the velocity resolution performance for the proposed methods as a function of the number of exploited multipath returns, we use the same setup as in the previous example. However, we vary the velocity difference between the two targets from 0.4 m/s to 2 m/s in steps of 0.4 m/s. We repeat the experiment 100 times and use a simplistic detection

scheme to obtain an upper bound on the performance assuming that the number of targets is known a priori. More specifically, for the reconstruction with joint velocity estimation, we choose the two strongest pixels and check if they correspond to the true target velocities. While in real life this detection scheme is not feasible, it serves as a suitable metric to provide a fair comparison for the examined cases. To quantify the performance of the two-step approach, i.e., reconstruction with subsequent velocity estimation, we calculate the root mean squared error (RMSE) of the velocity estimate. Furthermore, the detection rate is calculated, where an RMSE smaller than the velocity grid spacing, i.e., 0.2 m/s means successful detection. Fig. 10 summarizes the velocity estimation performance results. For various amounts of multipath, the detection performance for reconstruction with SparSA, BOMP, and the two-step method is shown in Figs. 10a-c, whereas Fig. 10d depicts the RMSE of the velocity estimation of the two-step method along with the 0.2 m/s threshold (dotted line). Note that the two-step method requires more than one propagation path to estimate the velocity vectors, hence, the case $R = 1$ is missing for this approach. We observe that without multipath exploitation, none of the methods is able to resolve closely-spaced velocities, while the resolution capabilities improve with increasing number of exploited multipath returns. For $R = 7$, all methods are able to separate velocity differences of 1.2 m/s and beyond. This is also reflected by the estima-
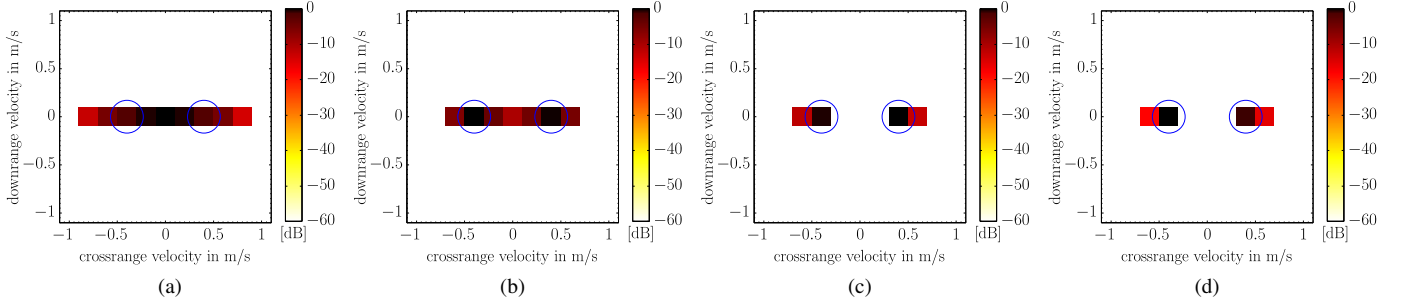
Fig. 9. CS reconstruction results for (a) direct path only ($R = 1$), (b) 1st order paths only ($R = 5$), (c) one 2nd order path ($R = 6$), and (d) all paths ($R = 7$).
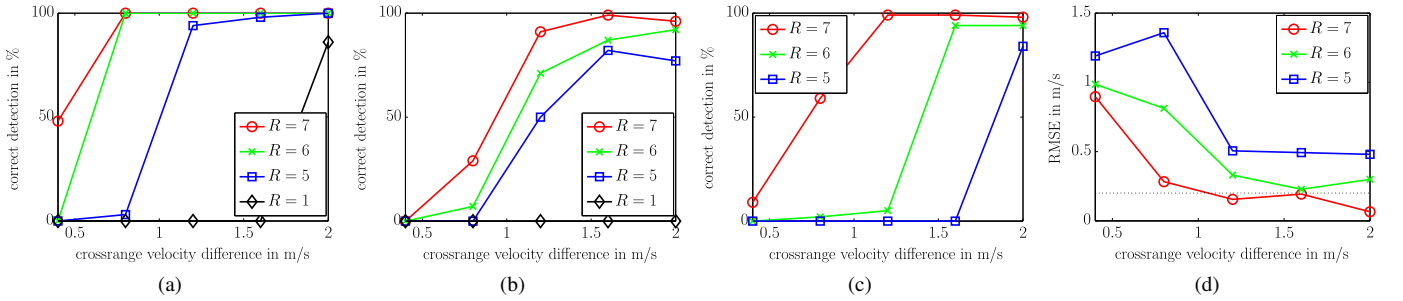

Fig. 10. Crossrange velocity resolution success for various amounts of multipath employing (a) CS using SparSA, (b) CS using BOMP, and (c) the two-step method. (d) RMSE for veocity estimation using the two-step method.

tion error plot of the two-step method, shown in Fig. 10d, wherein exploitation of more paths results in a lower RMSE. Furthermore, the resolution performance of the three methods scales with the computational complexity. While the two-step approach is computationally inexpensive, it performs rather poorly as compared to the other two methods, see Fig. 10c. When using the joint reconstruction with BOMP, refer to Fig. 10b, the performance improves at the expense of an increased computational complexity, whereas the numerically demanding SparSA reconstruction in Fig. 10a clearly provides the best performance. The results in Fig. 10 confirm that it is advantageous to exploit the information contained in the multipath returns for improved scene reconstruction.

3) Receiver Operating Characteristic Curves: Finally, we compare different scenarios and algorithms for TWRI by simulating the receiver operating characteristic (ROC) curves. We use the same multistatic radar geometry and scene setup with four targets as described in Section V-A1. The ROC curves for the considered multi-target scene have been calculated in the following manner. Simple amplitude detection is used to first form a binary image. A target pixel is considered to be correctly detected if the detected pixel coincides with the true target state or lies in one of the eight immediate neighboring pixels. This must be fulfilled for both the location and the velocity. Several detected pixels within this neighborhood are treated as one. A false alarm event is defined as a pixel detected outside the immediate neighborhood of any target. This corresponds to an unwanted clutter or ghost pixel in the image. The simulation results are averaged over 20 Monte Carlo runs and the corresponding ROC curves are averaged on a common false alarm axis. The realizations of the receiver
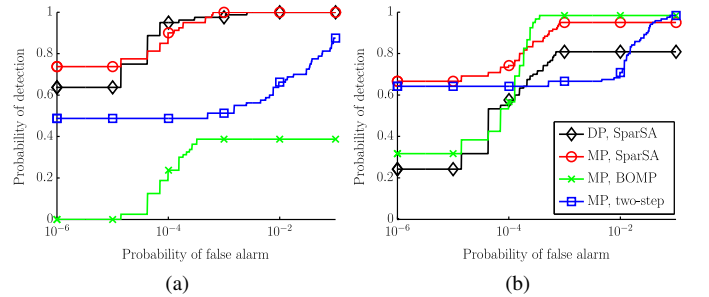

Fig. 11. ROC curves for various CS reconstruction methods (a) without and (b) including corner returns. The legend applies to both plots.

noise as well as the random downsampling matrices change across the various Monte Carlo runs.

In the first simulation, we consider only the target returns and do not include the room corner returns in the received signal. The undersampling parameters are selected as $T_{\text{d}} = 20$, $M_{\text{d}}N_{\text{d}} = 2$, and $K_{\text{d}} = 15$ and the following algorithms and multipath environments are considered:

- *DP, SparSA:* Only the direct path is modeled, i.e. $R = 1$ and conventional CS reconstruction using SparSA is employed.
- *MP, SparSA:* All $R = 7$ paths are modeled. CS based multipath exploitation using SparSA is employed.
- *MP, BOMP:* All $R = 7$ paths are modeled. CS based multipath exploitation using BOMP is employed.
- *MP, two-step:* All $R = 7$ paths are modeled. Two-step multipath exploitation is employed.

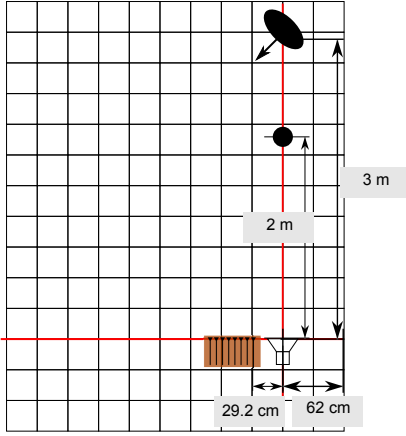Fig. 11a depicts the corresponding ROC curves. Considering

Fig. 12. Scene layout of a human (ellipse) walking diagonally towards the radar. Smaller stationary object (circle) resides at a closer downrange.

the multipath scenario, reconstruction using the optimization based approach ("MP, SparSA") performs best, followed by the two-step approach and the BOMP. Note that for the two-step approach, only the target location performance is considered in the ROC while velocity estimation is neglected, which may explain the advantage over the BOMP. The two reconstructions based on SparSA depict similar performance. Therefore, when exploited, multipath is neither disadvantageous nor advantageous in this simulation scenario.

In a second simulation, corner returns are added to the received signal. The number of used transceiver-pairs has been increased to $M_d N_d = 8$ to accommodate for the reduced sparsity in the reconstruction. The resulting ROC curves are presented in Fig. 11b. The locations of the corners are considered stationary targets when calculating the ROC. In this case, multipath is clearly a benefit rather than a nuisance. By exploiting the power of the target multipath, the detection performance can be improved in a scenario with strong stationary clutter. Both the SparSA and BOMP based multipath exploitation algorithms outperform reconstruction without multipath. The two-step approach, however, seems to suffer significantly from the corner clutter. Note that due to the reduced sparsity of the scene, the two SparSA methods fail to reconstruct all targets leading to an ROC that saturates at $P_D < 0$. This can be avoided by properly tuning the regularization parameter. However, we kept the same level of regularization throughout the results to maintain comparability.

B. Experimental Results

We present experimental results for a wideband real aperture pulse-Doppler radar with $M = 1$ transmitter and a uniform linear array with $N = 8$ receivers. The data has been recorded at the Radar Imaging Lab, Villanova University, in a semi-controlled lab environment. The transmit waveform is a modulated Gaussian pulse, covering the frequency range from 1.5 to 4.5 GHz. We recorded 768 fast time samples at a sampling rate $f_s = 7.68$ GHz and subsequently gated out the early and late returns to clean the data, resulting in $T = 153$ samples. The transmitter was placed 62 cm away from a side wall and the receive array (element spacing 6 cm)
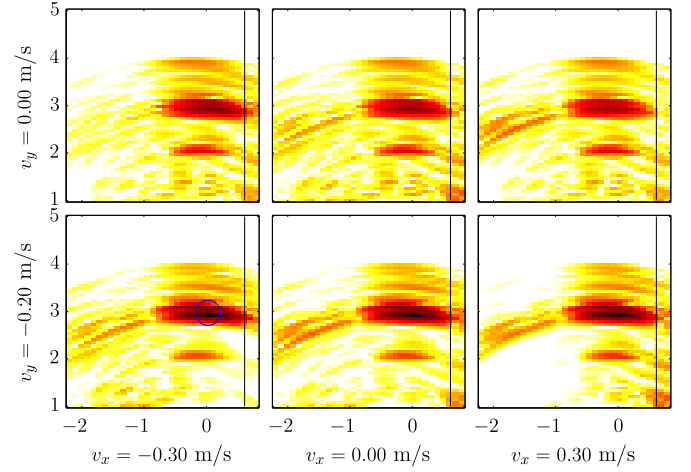

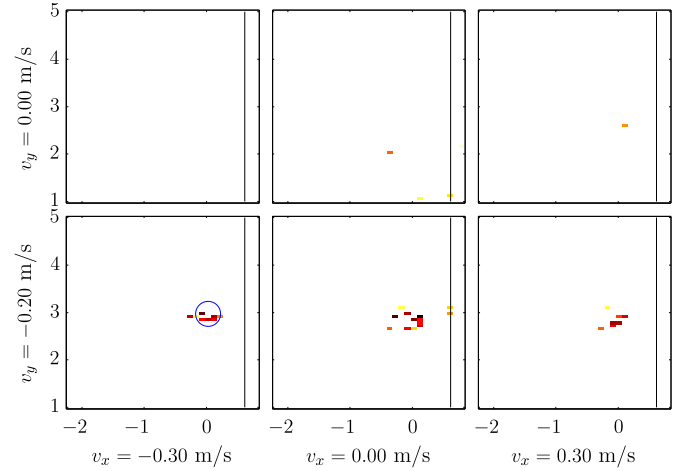Fig. 13. Delay and sum beamforming result of the walking human using full data

Fig. 14. CS reconstruction of the walking human using 20% of the measurements.

was placed on the other side of the transmitter at a distance (to the first receive array element) of 29.2 cm on the same baseline. No front wall was present in the scene. A total of $R = 4$ possible propagation paths are expected, namely, the direct path, two first order and one second order multipath via the side wall. The scene of interest is spatially discretized into a $N_x \times N_y = 32 \times 64$ pixel grid. The target velocities are discretized on an $N_{v_x} \times N_{v_y} = 5 \times 7$ grid spanning target velocity components between ± 0.6 m/s. A scenario with a human walking diagonally towards the radar was recorded. All of the above mentioned propagation paths are expected to be observed for the human. Refer to Fig. 12 for an illustration of the scene layout.

We first show the conventional beamforming results using full measurements in Fig. 13, where the beamformer for each spatial image has been matched to the corresponding target velocity. The expected position of the human is marked with a circle. It is evident that although both the human and the stationary target have been properly localized, the corresponding target velocities cannot be discerned from the beamformed images. Group sparse reconstruction using SparSA with 20%

of the full Nyquist measurements is shown in Fig. 14. The downsampling parameters of (21) are set to $T_{\mathrm{d}} = 50$, $N_{\mathrm{d}} = 5$ and $K_{\mathrm{d}} = 15$. In order to account for the higher amount of clutter and noise in the experimental data, the downsampling factor in the fast time domain has been decreased as compared to that used in the simulations. For the same reason, we increase the regularization parameter to $\mu_{\mathrm{norm}} = 0.3$. The human as a moving target is recovered with approximately correct location and velocities, with the direction of the movement consistent with the ground truth. There is some leakage in the neighboring velocity cell, owing to the high coherence in the measurement matrix and also due to the complex nature of torso and limb movements. Additionally, some residual clutter in the stationary image can be observed. This is attributed to a small stationary objects present in the scene (see Fig. 12). Group sparse reconstruction using BOMP and the two-step approach were also used for scene reconstruction (corresponding images are omitted for brevity). BOMP-based approach failed to accurately reconstruct the scene and exhibited a much higher amount of clutter. The reconstruction results using the two-step approach also exhibited larger background noise and lower signal-to-clutter ratio.

VI. CONCLUSION

In this paper, we presented a forward linear model under multipath propagation for simultaneous localization of stationary and moving targets behind walls. We considered multistatic radar operation, with time-division multiplexing of the transmitters for data acquisition. Based on the presented model, we proposed a group sparse reconstruction approach to solve the inverse problem under reduced data volume. In this way, we are able to recover the locations and velocities of indoor targets from much fewer than Nyquist measurements without multipath ghosting effects. We also proposed a computationally inexpensive two-step scheme that first obtains the target locations via sparse reconstruction and subsequently exploits multipath to estimate the target velocity vector using conventional Doppler processing. Supporting simulation and experimental results are provided, which demonstrate that highly-resolved, ghost-suppressed target information is obtained from few measurements using the proposed schemes.

It is noted that the proposed method is intended for real-time location and velocity estimation of targets. However, existing conventional processing hardware is not capable of solving CS reconstruction problems fast enough for joint location and velocity estimations. The two-step approach is an attempt to reduce the computational complexity of sparsity-based localization and velocity estimation, thus rendering real-time implementations feasible.

REFERENCES

[1] M. Amin, Ed., *Through-the-Wall Radar Imaging*. Boca Raton, FL: CRC Press, 2011.

[2] M. Amin, Ed., *Compressive Sensing for Urban Radar*. Boca Raton, FL: CRC Press, 2015.

[3] C. Le, T. Dogaru, L. Nguyen, and M. Ressler, "Ultrawideband (UWB) radar imaging of building interior: Measurements and predictions," *IEEE Transactions on Geoscience and Remote Sensing*, vol. 47, no. 5, pp. 1409–1420, May 2009.

[4] F. Soldovieri and R. Solimene, "Through-wall imaging via a linear inverse scattering algorithm," *IEEE Geoscience and Remote Sensing Letters*, vol. 4, no. 4, pp. 513–517, Oct. 2007.

[5] M. Dehmollaian and K. Sarabandi, "Refocusing through building walls using synthetic aperture radar," *IEEE Transactions on Geoscience and Remote Sensing*, vol. 46, no. 6, pp. 1589–1599, Jun. 2008.

[6] F. Ahmad, M. Amin, and P. Zemany, "Dual-frequency radars for target localization in urban sensing," *IEEE Transactions on Aerospace and Electronic Systems*, vol. 45, no. 4, pp. 1598–1609, Oct. 2009.

[7] C.-P. Lai and R. Narayanan, "Ultrawideband random noise radar design for through-wall surveillance," *IEEE Transactions on Aerospace and Electronic Systems*, vol. 46, no. 4, pp. 1716–1730, Oct. 2010.

[8] C. Debes, J. Hahn, A. Zoubir, and M. Amin, "Target discrimination and classification in through-the-wall radar imaging," *IEEE Transactions on Signal Processing*, vol. 59, no. 10, pp. 4664–4676, Oct. 2011.

[9] M. Leigsnering, M. Amin, F. Ahmad, and A. Zoubir, "Multipath exploitation and suppression for SAR imaging of building interiors: An overview of recent advances," *IEEE Signal Processing Magazine*, vol. 31, no. 4, pp. 110–119, Jul. 2014.

[10] Y.-S. Yoon and M. Amin, "Compressed sensing technique for high-resolution radar imaging," in *Proceedings of SPIE Signal Processing, Sensor Fusion, and Target Recognition XVII*, vol. 6968, no. 1, Orlando, FL, Mar. 2008, p. 69681A.

[11] M. Leigsnering, C. Debes, and A. Zoubir, "Compressive sensing in through-the-wall radar imaging," in *IEEE International Conference on Acoustics, Speech and Signal Processing (ICASSP)*, Prague, Czech Republic, May 2011, pp. 4008–4011.

[12] Q. Huang, L. Qu, B. Wu, and G. Fang, "UWB through-wall imaging based on compressive sensing," *IEEE Transactions on Geoscience and Remote Sensing*, vol. 48, no. 3, pp. 1408–1415, Mar. 2010.

[13] F. Ahmad and M. G. Amin, "Through-the-wall human motion indication using sparsity-driven change detection," *IEEE Transactions on Geoscience and Remote Sensing*, vol. 51, no. 2, pp. 881–890, Feb. 2013.

[14] J. Qian, F. Ahmad, and M. G. Amin, "Joint localization of stationary and moving targets behind walls using sparse scene recovery," *Journal of Electronic Imaging*, vol. 22, no. 2, p. 021002, Jun. 2013.

[15] V. Dang and O. Kilic, "Joint DoA-range-doppler tracking of moving targets based on compressive sensing," in *IEEE International Symposium on Antennas and Propagation and USNC-URSI Radio Science Meeting*, Memphis, TN, Jul. 2014, pp. 141–142.

[16] S. Kidera, T. Sakamoto, and T. Sato, "Extended imaging algorithm based on aperture synthesis with double-scattered waves for UWB radars," *IEEE Transactions on Geoscience and Remote Sensing*, vol. 49, no. 12, pp. 5128–5139, Dec. 2011.

[17] P. Setlur, M. Amin, and F. Ahmad, "Multipath model and exploitation in through-the-wall and urban radar sensing," *IEEE Transactions on Geoscience and Remote Sensing*, vol. 49, no. 10, pp. 4021–4034, Oct. 2011.

[18] G. Gennarelli, G. Riccio, R. Solimene, and F. Soldovieri, "Radar imaging through a building corner," *IEEE Transactions on Geoscience and Remote Sensing*, vol. 52, no. 10, pp. 6750–6761, Oct. 2014.

[19] G. Gennarelli and F. Soldovieri, "Radar imaging through cinderblock walls: Achievable performance by a model-corrected linear inverse scattering approach," *IEEE Transactions on Geoscience and Remote Sensing*, vol. 52, no. 10, pp. 6738–6749, Oct. 2014.

[20] M. Leigsnering, F. Ahmad, M. Amin, and A. Zoubir, "Multipath exploitation in through-the-wall radar imaging using sparse reconstruction," *IEEE Transactions on Aerospace and Electronic Systems*, vol. 50, no. 2, pp. 920–939, Apr. 2014.

[21] G. Gennarelli, I. Catapano, and F. Soldovieri, "RF/microwave imaging of sparse targets in urban areas," *IEEE Antennas and Wireless Propagation Letters*, vol. 12, pp. 643–646, May 2013.

[22] Y. Yu, A. Petropulu, and H. Poor, "MIMO radar using compressive sampling," *IEEE Journal of Selected Topics in Signal Processing*, vol. 4, no. 1, pp. 146–163, Feb. 2010.

[23] X. Chen, H. Leung, and M. Tian, "Multitarget detection and tracking for through-the-wall radars," *IEEE Transactions on Aerospace and Electronic Systems*, vol. 50, no. 2, pp. 1403–1415, Apr. 2014.

[24] F. Ahmad and M. Amin, "Multi-location wideband synthetic aperture imaging for urban sensing applications," *Journal of the Franklin Institute*, vol. 345, no. 6, pp. 618–639, Sep. 2008.

[25] L. Potter, E. Ertin, J. Parker, and M. Cetin, "Sparsity and compressed sensing in radar imaging," *Proceedings of the IEEE*, vol. 98, no. 6, pp. 1006–1020, june 2010.

[26] J. Jackson, B. Rigling, and R. Moses, "Canonical scattering feature models for 3D and bistatic SAR," *IEEE Transactions on Aerospace and Electronic Systems*, vol. 46, no. 2, pp. 525–541, Apr. 2010.

[27] Y.-S. Yoon and M. Amin, "Spatial filtering for wall-clutter mitigation in through-the-wall radar imaging," *IEEE Transactions on Geoscience and Remote Sensing*, vol. 47, no. 9, pp. 3192–3208, Sep. 2009.

[28] F. H. C. Tivive, A. Bouzerdoum, and M. G. Amin, "An SVD-based approach for mitigating wall reflections in through-the-wall radar imaging," in *IEEE Radar Conference (RADAR)*, Kansas City, MO, May 2011, pp. 519–524.

[29] E. Lagunas, M. G. Amin, F. Ahmad, and M. Nájar, "Joint wall mitigation and compressive sensing for indoor image reconstruction," *IEEE Transactions on Geoscience and Remote Sensing*, vol. 51, no. 2, pp. 891–906, Feb. 2013.

[30] M. Soumekh, *Synthetic Aperture Radar Signal Processing with MATLAB Algorithms*. New York, NY: John Wiley and Sons, 1999.

[31] F. Ahmad, M. Amin, and S. Kassam, "A beamforming approach to stepped-frequency synthetic aperture through-the-wall radar imaging," in *IEEE Int. Workshop on Computational Advances in Multi-Sensor Adaptive Processing*, Puerto Vallarta, Mexico, Dec. 2005, pp. 24–27.

[32] M. A. Richards, J. A. Scheer, and W. A. Holm, Eds., *Principles of Modern Radar: Basic Principles*. Raleigh, NC: SciTech Publishing, 2010.

[33] M. Leigsnering, F. Ahmad, M. Amin, and A. Zoubir, "CS based specular multipath exploitation in TWRI under wall position uncertainties," in *IEEE Sensor Array and Multichannel Signal Processing Workshop (SAM)*, A Coruña, Spain, Jun. 2014, pp. 481–484.

[34] A. Petropulu, Y. Yu, and J. Huang, "On exploring sparsity in widely separated MIMO radar," in *Conference Record of the Forty Fifth Asilomar Conference on Signals, Systems and Computers (ASILOMAR)*, Pacific Grove, CA, Nov. 2011, pp. 1496–1500.

[35] M. Leigsnering, F. Ahmad, M. Amin, and A. Zoubir, "Specular multipath exploitation for improved velocity estimation in through-the-wall radar imaging," in *IEEE International Conference on Acoustics, Speech, and Signal Processing (ICASSP)*, Florence, Italy, May 2014, pp. 1060–1064.

[36] A. Gurbuz, J. McClellan, and W. Scott, "Compressive sensing for subsurface imaging using ground penetrating radar," *Signal Processing*, vol. 89, no. 10, pp. 1959–1972, Oct. 2009.

[37] S. Wright, R. Nowak, and M. Figueiredo, "Sparse reconstruction by separable approximation," *IEEE Transactions on Signal Processing*, vol. 57, no. 7, pp. 2479–2493, Jul. 2009.

[38] Y. Eldar, P. Kuppinger, and H. Bolcskei, "Block-sparse signals: Uncertainty relations and efficient recovery," *IEEE Transactions on Signal Processing*, vol. 58, no. 6, pp. 3042–3054, Jun. 2010.

[39] R. Baraniuk, V. Cevher, M. Duarte, and C. Hegde, "Model-based compressive sensing," *IEEE Transactions on Information Theory*, vol. 56, pp. 1982–2001, Apr. 2010.

[40] W. Deng, W. Yin, and Y. Zhang, "Group sparse optimization by alternating direction method," Department of Computational and Applied Mathematics, Rice University, Technical Report TR11-06, 2011.

[41] M. Davenport, J. Laska, J. Treichler, and R. Baraniuk, "The pros and cons of compressive sensing for wideband signal acquisition: Noise folding versus dynamic range," *IEEE Transactions on Signal Processing*, vol. 60, no. 9, pp. 4628–4642, Sep. 2012.

Fauzia Ahmad (S'97 – M'97 – SM'06) received her Ph.D. degree in electrical engineering from the University of Pennsylvania, Philadelphia, PA in 1997. Since 2002, she has been with the Villanova University, Villanova, PA, where she is currently a Research Professor with the Center for Advanced Communications in the College of Engineering, and is the Director of the Radar Imaging Laboratory. She is a Senior Member of the Institute of Electrical and Electronics Engineers (IEEE), 2006 and a Senior Member of the International Society for Optics and Photonics (SPIE), 2012. Dr. Ahmad is an Associate Editor of the IEEE TRANSACTIONS ON SIGNAL PROCESSING. She also serves on the Editorial Boards of the IET Radar, Sonar & Navigation and the SPIE/IS&T Journal of Electronic Imaging. She is a member of the IEEE Aerospace and Electronic System Society's Radar Systems Panel. Her general research interests are in the areas of radar imaging, radar signal processing, statistical signal and array processing, compressive sensing, waveform diversity and design, target localization and tracking, and ultrasound imaging. She has published more than 170 journal articles and peer-reviewed conference papers and five book chapters in the aforementioned areas.
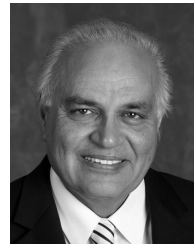
Moeness G. Amin (F'01) received his Ph.D. degree in 1984 from University of Colorado, Boulder. He has been on the Faculty of the Department of Electrical and Computer Engineering at Villanova University since 1985, where he is now a Professor and the Director of the Center for Advanced Communications. Dr. Amin is a Fellow of IEEE, SPIE, IET and EURASIP. He is a Recipient of the IEEE Third Millennium Medal, the EURASIP Individual Technical Achievement Award and the IEEE Signal Processing Society Technical Achievement Award. He was a Distinguished Lecturer of the IEEE Signal Processing Society. Dr. Amin has over 700 publications in the field of signal and array processing, including radar imaging. He authored and co-authored 18 book chapters and is the editor of the two books from CRC Press: "Through the Wall Radar Imaging" (2011) and "Compressive Sensing for Urban Radar" (2014). He is a recipient of eight best paper awards. He serves on the IEEE Signal Processing Magazine and Signal Processing Journal Editorial Boards.

Abdelhak M. Zoubir (F'08) received his Dr.-Ing. degree from Ruhr-Universität Bochum, Germany. He was with Queensland University of Technology, Australia, from 1992 to 1998. He then joined Curtin University of Technology, Australia, as a Professor of Telecommunications and was interim Head of the School of Electrical and Computer Engineering from 2001 to 2003. Since 2003, he has been a Professor of Signal Processing at Technische Universität Darmstadt, Germany. He is a Fellow of IEEE, an IEEE Distinguished Lecturer (Class of 2010–2011), Past-Chair of the Signal Processing Theory and Methods Technical Committee of the IEEE Signal Processing Society, and the Editor-in-Chief of the IEEE Signal Processing Magazine from 2012–2014. He served on the Editorial Boards of various journals of the IEEE and the European Association of Signal Processing (EURASIP). He currently serves on the Board of Directors of the EURASIP. His research interest lies in statistical methods for signal processing applied to telecommunications, radar, sonar, car engine monitoring, and biomedicine. He has published over 300 papers in these areas.

Michael Leigsnering (S'11) received the Dipl.-Ing. degree in electrical engineering and information technology from the Technische Universität Darmstadt in 2010. He is currently working towards his Ph.D. degree in the Signal Processing Group, Institute of Telecommunications, Technische Universität Darmstadt. His research interest lies in array signal processing with focus on through-the-wall radar imaging, compressive sensing, and multipath phenomena. He has been a visitor at Center for Advanced Communications, Villanova University, Villanova, PA in 2012, 2013 and 2014.